Model-Based Sensorless Control of an IPMSM With Enhanced Robustness Against Load Disturbances Based on Position and Speed Estimator Using a Speed Error

Younggi Lee, *Student Member, IEEE*, and Seung-Ki Sul, *Fellow, IEEE*

***Abstract*—In this paper, new model-based sensorless control methods are proposed that include independent estimations of position and speed errors, and compatible position and speed estimators. Using the proposed position estimator, a unity transfer function can be achieved from the actual position to the estimated position, eliminating the effects of load disturbances. This implies that the position error would ideally be zero, even in a transient state. In addition, the effects of parameter and voltage synthesis errors on the steady-state position error are analyzed. Experimental results verify both the analysis and the effectiveness of the proposed methods under severe load disturbances such as speed transient (20 000 r/min/s) and load torque transient (10 p.u./s). With the proposed methods, position estimation errors are significantly reduced by more than 50% during speed and load torque transients at identical dominant-pole placements, verifying the enhanced tracking capability and robustness of the proposed methods against external load disturbances.**

***Index Terms*—Interior permanent magnet synchronous motor (IPMSM), model-based sensorless control, position and speed estimator, robustness, speed error.**

NOMENCLATURE

Superscript "r"	Rotor reference frame.
Superscript "$\hat{r}$"	Estimated rotor reference frame.
θ_r, ω_r	Rotor position and speed in electrical angle.
$\hat{\theta}_r$, $\hat{\omega}_r$	Estimated values of θ_r and ω_r.
$\tilde{\theta}_r$, $\tilde{\omega}_r$	Position and speed estimation errors.
v_{ds}^r, v_{qs}^r	d and q components of the stator input voltage in the rotor reference frame.
i_{ds}^r, i_{qs}^r	d and q components of the input current in the rotor reference frame.
R_s	Stator winding resistance.
λ_f	Flux linkage from permanent magnets.
L_{ds}, L_{qs}	Synchronous inductances on the d and q axes.
J_m	Moment of inertia.
B_m	Friction coefficient.
T_e, $T_{\rm load}$	Electric torque and load torque.
P	Number of poles.
p	Differential operator.

Manuscript received July 3, 2017; revised September 27, 2017; accepted November 14, 2017. Date of publication November 22, 2017; date of current version March 19, 2018. Paper 2017-IDC-0631.R1, presented at the 2016 IEEE Symposium on Sensorless Control for Electrical Drives, Nadi, Fiji, Jun. 5–6, and approved for publication in the IEEE TRANSACTIONS ON INDUSTRY APPLICATIONS by the Industrial Drives Committee of the IEEE Industry Applications Society. This work was supported by the Seoul National University Electric Power Research Institute. *(Corresponding author: Younggi Lee.)*

Y. Lee is with Department of Electrical and Computer Engineering, Seoul National University, Seoul 08826, South Korea (e-mail: younggi@snu.ac.kr).

S.-K. Sul is with Department of Electrical and Computer Engineering, Seoul National University, Seoul 08826, South Korea (e-mail: sulsk@plaza.snu.ac.kr).

Color versions of one or more of the figures in this paper are available online at http://ieeexplore.ieee.org.

Digital Object Identifier 10.1109/TIA.2017.2777390

I. INTRODUCTION

SENSORLESS control of an interior permanent magnet synchronous motor (IPMSM) has been widely used in various drive applications, including home appliances, robots, and traction systems, due to the various studies and commercialization efforts that have taken place. Considering that the advantages of sensorless control method, such as costs and volumes, and the increased reliability are attractive, many approaches to estimate rotor position and speed without a position sensor have been developed over the past few decades [1]–[34].

Sensorless control methods of an AC motor can generally be divided into two categories: 1) high-frequency signal injection methods [1]–[11]; and 2) model-based methods [8]–[34]. The former are based on magnetic saliency and are commonly used in standstill and low-speed operations. However, because the operating speed is limited and an additional loss is imposed due to the injection voltage, the latter methods are preferred in high-speed operations.

In both of these sensorless methods, accurate estimation performance and increased control bandwidths have always been the important issues. For an accurate estimation of the rotor position, research has shown that the voltage distortion by the inverter should be compensated, as the distorted voltage leads to position estimation errors [6]–[8], [12]–[16]. In addition, improved estimation performance can be realized if cross coupling and nonlinearly varying inductances from saturation and the mechanical structure are considered [2]–[4], [15]–[17]. Elaborate machine model using flux or the concept of the extended electromotive force (EEMF) [18]–[21] and online parameter identification schemes [12], [22], [35]

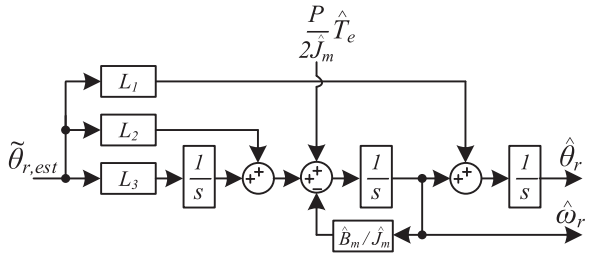

Fig. 1. Position and speed estimator with modified speed output.

would be other viable solutions to ensure accurate position estimation.

Meanwhile, regarding the increased control bandwidth, the position and speed estimator that reflects mechanical relationship has been proposed [23]. In [23], by inserting a torque feedforward input into the estimator, the estimation bandwidth can be increased in sensorless speed control. This scheme can be applied to the high-frequency signal injection methods as well in the same manner [5], [6]. In [5], the estimator in [23] was modified such that the estimated speed is represented as the output of an integrator, as shown in Fig. 1. In [5], along with square-wave signal injection, the overall bandwidth of the system, including the position, speed, and current control, can be extended by removing two low-pass filters.

Despite continuous efforts to enhance the control performance, sensorless control methods remain vulnerable to external disturbances such as speed variations in the current control mode and load torque variations in the speed control mode. Even if robustness against external loads is one of the most important characteristics in actual sensorless control, especially for servo applications, it remains as a weak point because external disturbances are not known in most cases. Naturally, there have been approaches to neutralize load disturbances as well [11], [24], [36]. However, the estimated loads in [24] and [36] have been used to improve the speed control performance by revising the current reference rather than estimating the position and speed. Meanwhile, effective disturbance rejection performance was presented in [11], but the transient was not severe as much as that in this paper. Other studies in [25], [26], and [35] have shown that robustness against parameter variations and voltage synthesis errors can be increased.

This paper, therefore, focuses on robust estimations of the position and speed against external load disturbances based on a model-based sensorless control. The key contributions of this paper are independent estimations of position and speed errors and the proposal of two compatible position and speed estimators. This topic has already been covered in [27], and it has been shown that the estimation performance in a severe transient state can be improved. However, the estimator proposed in [27] is prone to steady-state speed error with parameter errors. Moreover, because the position estimation error is dependent on the estimator gain, it should be considered as well as the dynamic characteristics during the gain-setting procedure.

Considering these issues, the position and speed estimator proposed in this paper is improved from that in [27] by adding an additional state, which can nullify the speed error and separate the position error from the estimator gains. In addition, the effects of parameter and voltage synthesis errors on the steady-state position error are analyzed and verified by experimental results. Although the classical papers presented sensorless methods using the speed (or EMF) error information [28], [29], their concepts regarding the speed error are different from that in this paper. From this reason, several terms that are important in highly dynamic operations were neglected in previous research.

Using the proposed position estimator, a unity transfer function can be achieved from the actual position to the estimated position, eliminating the effects of load disturbances. This indicates that the position error would ideally be zero, even in a transient state. Experimental results verify the effectiveness of the proposed methods under severe load disturbances such as speed transient (20000 r/min/s) and load torque transient (10 p.u./s). With the proposed methods, the maximum position estimation error is conspicuously reduced by 70% during speed transient and by 50% during load torque transient under identical dominant-pole placements, verifying the enhanced tracking capability and robustness of the proposed methods in high- and low-speed conditions.

II. Conventional Model Based Sensorless Control

In medium- and high-speed regions, the rotor position and speed are mainly estimated by model-based methods because the required information is included in the back-EMF voltages. In this section, conventional model-based sensorless methods are introduced. The first uses an EEMF and the second uses a speed error, which is similar to the proposed method in this paper.

The fundamental model of a PMSM can be represented in the rotor reference frame by (1), where d-axis is aligned with the direction of the magnetic north pole of the rotor $(= \theta_r)$

$$\begin{bmatrix} v_{ds}^r \\ v_{qs}^r \end{bmatrix} = \begin{bmatrix} R_s & -\omega_r L_{qs} \\ \omega_r L_{ds} & R_s \end{bmatrix} \begin{bmatrix} i_{ds}^r \\ i_{qs}^r \end{bmatrix} + \begin{bmatrix} L_{ds} & 0 \\ 0 & L_{qs} \end{bmatrix} p \begin{bmatrix} i_{ds}^r \\ i_{qs}^r \end{bmatrix} + \begin{bmatrix} 0 \\ \omega_r \lambda_f \end{bmatrix}. \quad (1)$$

In (1), it is assumed that the cross-coupling inductances between d and q axes are sufficiently small.

For sensorless control, (1) should be expressed in the estimated rotor reference frame because every control is based on the estimated position. However, it can be noticed from (15) in the appendix that much complicated terms are induced from coupling terms due to the saliency in a motor, i.e., $L_{\rm ds} \neq L_{\rm qs}$.

To simplify the expression in the estimated frame, (1) can be rearranged as (2) with the introduction of the EEMF concept, $E_{\rm ex}$ [20], [21]

$$\begin{bmatrix} v_{ds}^r \\ v_{qs}^r \end{bmatrix} = \begin{bmatrix} R_s & -\omega_r L_{qs} \\ \omega_r L_{qs} & R_s \end{bmatrix} \begin{bmatrix} i_{ds}^r \\ i_{qs}^r \end{bmatrix} + \begin{bmatrix} L_{ds} & 0 \\ 0 & L_{ds} \end{bmatrix} p \begin{bmatrix} i_{ds}^r \\ i_{qs}^r \end{bmatrix} + \begin{bmatrix} 0 \\ E_{\rm ex} \end{bmatrix} \quad (2)$$

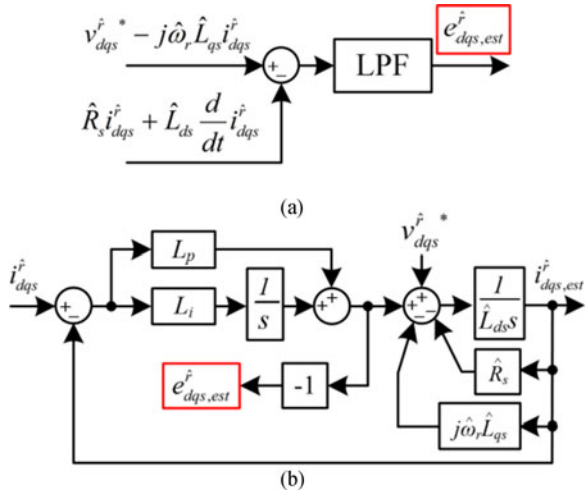

Fig. 2. Conventional EEMF estimator. (a) Using a disturbance estimator with a low-pass filter. (b) Using a PI-type state filter.

where $E_{\rm ex} \equiv \omega_r \lambda_f + 2\omega_r \Delta L_s i^r_{ds} - 2\Delta L_s p i^r_{qs}$ and ΔL_s is defined as $(L_{ds} - L_{qs})/2$. The voltage equation of the IPMSM is then expressed as if the inductance matrices were symmetric. Similarly, (2) can be expressed in the estimated frame by the following equation:

$$\begin{bmatrix} v^{\hat{r}}_{ds} \\ v^{\hat{r}}_{qs} \end{bmatrix} = \begin{bmatrix} R_s & -\omega_r L_{qs} \\ \omega_r L_{qs} & R_s \end{bmatrix} \begin{bmatrix} i^{\hat{r}}_{ds} \\ i^{\hat{r}}_{qs} \end{bmatrix} + \begin{bmatrix} L_{ds} & 0 \\ 0 & L_{ds} \end{bmatrix} p \begin{bmatrix} i^{\hat{r}}_{ds} \\ i^{\hat{r}}_{qs} \end{bmatrix} + \begin{bmatrix} e^{\hat{r}}_{ds} \\ e^{\hat{r}}_{qs} \end{bmatrix} \tag{3}$$

where $\begin{bmatrix} e^{\hat{r}}_{ds} \\ e^{\hat{r}}_{qs} \end{bmatrix} = E_{\rm ex} \begin{bmatrix} -\sin\tilde{\theta}_r \\ \cos\tilde{\theta}_r \end{bmatrix} + L_{ds}(\omega_r - \hat{\omega}_r) \begin{bmatrix} i^{\hat{r}}_{qs} \\ -i^{\hat{r}}_{ds} \end{bmatrix}$.

Based on (3), various types of EEMF estimators have been proposed under the assumption that $\tilde{\omega}_r \equiv \omega_r - \hat{\omega}_r \approx 0$ [12], [20], [21], [23]. Among them are the two classical estimators shown in Fig. 2, where it has been disclosed that the dynamic characteristics of the estimators in Fig. 2(a) and (b) are identical [15]. In this paper, for straightforward implementation, the estimated EEMF $e^{\hat{r}}_{dqs,\rm est}$ is determined by Fig. 2(a).

For estimation of the position and speed, a Proportional–Integral–Derivative (PID)-type position and speed estimator including a torque feedforward input in Fig. 1 is commonly used [5], [6]. The estimator in Fig. 1 obtains input $\tilde{\theta}_{r,\rm est}$ from $e^{\hat{r}}_{dqs,\rm est}$ after the simple algebraic manipulation expressed in the following equation [20]:

$$\tilde{\theta}_{r,\rm est} = \tan^{-1}\left(-\frac{e^{\hat{r}}_{ds}}{e^{\hat{r}}_{qs}}\right) \text{ or } -\frac{e^{\hat{r}}_{ds}}{\hat{E}_{\rm ex}}. \tag{4}$$

Subsequently, the position and speed estimator adjusts the estimated position $\hat{\theta}_r$ and speed $\hat{\omega}_r$ in the direction that $\tilde{\theta}_{r,\rm est}$ is nullified.

On the other hand, classical papers discussed sensorless methods using speed or EMF error for nonsalient machines $(L_s = L_{ds} = L_{qs})$ [28], [29]. In these papers, the position and speed (or EMF) errors were estimated based on the difference between the measured and estimated current variations at two consecutive sampling points, i.e., $\Delta i^{\hat{r}}_{dqs} - \Delta i^{\hat{r}}_{dqs,\rm est}$. The exact expression of the difference can be deduced as follows:

$$\begin{bmatrix} \Delta i^{\hat{r}}_{ds} \\ \Delta i^{\hat{r}}_{qs} \end{bmatrix} - \begin{bmatrix} \Delta i^{\hat{r}}_{ds,\rm est} \\ \Delta i^{\hat{r}}_{qs,\rm est} \end{bmatrix} = \frac{T_{\rm samp}}{L_s} \begin{pmatrix} \lambda_f \begin{bmatrix} \omega_r \sin\tilde{\theta}_r \\ \hat{\omega}_r - \omega_r \cos\tilde{\theta}_r \end{bmatrix} \\ + L_s p\tilde{\theta}_r \begin{bmatrix} 0 & -1 \\ 1 & 0 \end{bmatrix} \begin{bmatrix} i^{\hat{r}}_{ds} \\ i^{\hat{r}}_{qs} \end{bmatrix} \\ + L_s \begin{bmatrix} 0 & -\hat{\omega}_r + \omega_r \\ \hat{\omega}_r - \omega_r & 0 \end{bmatrix} \begin{bmatrix} i^{\hat{r}}_{ds} \\ i^{\hat{r}}_{qs} \end{bmatrix} \end{pmatrix}. \tag{5}$$

In this equation, no parameter errors and ideal voltage synthesis were assumed. However, despite these assumptions, previous studies estimated position and speed errors while neglecting the last two terms or considering only one of them in (5). For the first case of neglecting the last two terms, even if they appear to cancel out each other, this is not true in all cases, such as the case shown in Fig. 1, where differentiation of the estimated position differs from the estimated speed. Thus, excluding these terms leads to inaccurate estimations during dynamic operation such as rapid speed variations or abrupt load disturbances.

III. Proposed Estimation Method for Position and Speed Errors

In this paper, position and speed errors are estimated based on (16) in the appendix, where (16) is the linearized form of (15) under the assumptions that $\tilde{\theta}_r$ is less than 30 °E. Additionally, the speed term in (15) has been separated into the estimated and error terms, i.e., $\omega_r = \hat{\omega}_r + \tilde{\omega}_r$, which is the most important concept in this paper, as the actual speed as well as the position cannot be used in sensorless operations. By means of this separation step, $\tilde{\theta}_r$ and $\tilde{\omega}_r$ can be utilized for improved sensorless control after they are estimated from $\tilde{e}^{\hat{r}}_{dqs}$ in (16).

The errors are estimated by (6), which can be easily derived from (16)

$$\begin{bmatrix} \tilde{\omega}_{r,\rm est} \\ \tilde{\theta}_{r,\rm est} \end{bmatrix} = \frac{1}{D} \left(\begin{bmatrix} \lambda_{p\theta,q} & -\lambda_{p\theta,d} \\ 0 & 0 \end{bmatrix} \cdot s \begin{bmatrix} \tilde{e}^{\hat{r}}_{ds} \\ \tilde{e}^{\hat{r}}_{qs} \end{bmatrix} + \begin{bmatrix} e_{\theta,q} & -e_{\theta,d} \\ -\lambda_{\omega,q} & \lambda_{\omega,d} \end{bmatrix} \begin{bmatrix} \tilde{e}^{\hat{r}}_{ds} \\ \tilde{e}^{\hat{r}}_{qs} \end{bmatrix} \right) \tag{6}$$

where $D = (\lambda_{\omega,\rm d} \cdot \lambda_{\rm p\theta,q} - \lambda_{\omega,\rm q} \cdot \lambda_{\rm p\theta,d}) \cdot s + (\lambda_{\omega,\rm d} \cdot e_{\theta,\rm q} - \lambda_{\omega,\rm q} \cdot e_{\theta,\rm d})$. In addition, $e_{\theta,\rm d}$, $e_{\theta,\rm q}$, $\lambda_{\rm p\theta,d}$, $\lambda_{\rm p\theta,q}$, $\lambda_{\omega,\rm d}$, and $\lambda_{\omega,\rm q}$ are presented in detail in (16) in the appendix. In the mathematical model in (6), because the derivative of $\tilde{e}^{\hat{r}}_{dqs}$ is required to calculate $\tilde{\theta}_{r,\rm est}$ and $\tilde{\omega}_{r,\rm est}$, a simple estimation method is introduced in Fig. 3, rather than direct differentiation. In this way, a filtered form of $e^{\hat{r}}_{dqs,\rm est}$, i.e., $e^{\hat{r}\prime}_{dqs,\rm est}$ and its derivative, $s \cdot e^{\hat{r}\prime}_{dqs,\rm est}$, are obtained. In the experiment, $L_{\rm e}$, referring to the cut-off frequency of the estimator, was set to $2\pi \cdot 100$. How-

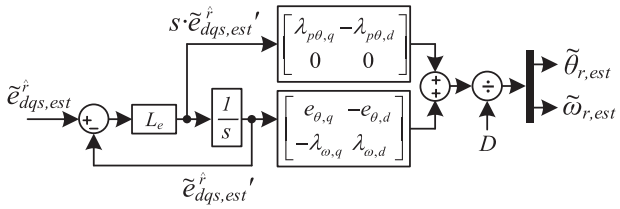

Fig. 3. Block diagram of the proposed estimation method for position and speed errors.

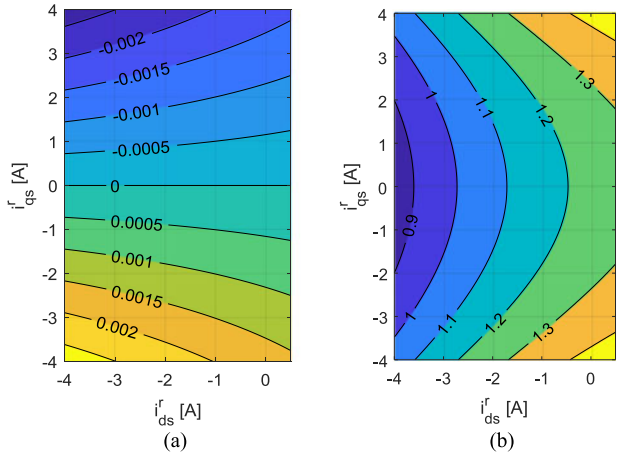

Fig. 4. Comparison of the coefficients in D at 1000 r/min. (a) Coefficient of the first-order term. (b) Coefficient of the zero-order term.

TABLE I
PARAMETERS OF THE IPMSM

IPMSM parameter	Value
Rated power	300 W
Rated current	2.85 A_{rms}
Pole number	6
Back-EMF constant	0.0626 V·s
Winding resistance $(R_s + R_{\rm inv})$	0.675 Ω
Synchronous inductances	L_{ds} : 7.15 mH, L_{qs} : 10.6 mH

ever, the dynamic characteristics in the denominator are ignored because it can cause stability problems depending on the operating condition. For this reason, only the zero-order term in D is considered. This scheme can be justified by Fig. 4, which shows that the first-order term is sufficiently small in all operating areas of the motor described in Table I, even under dynamic operations of several tens of Hz.

One noticeable point in the estimation is that the minimum speed is always required for the estimation, which is common in model-based sensorless control methods, because $\hat{\omega}_r$ is included in both $e_{\theta,d}$ and $e_{\theta,q}$ in the denominator. Therefore, a more suitable sensorless control method is preferred, such as a high-frequency signal injection method under certain speeds.

IV. Proposed Position and Speed Estimator

A. Design of the Estimator

Conventional position and speed estimators such as that shown in Fig. 1 are not appropriate for using the estimated

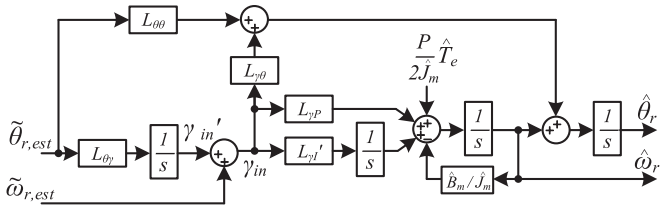

Fig. 5. Proposed position and speed estimator.

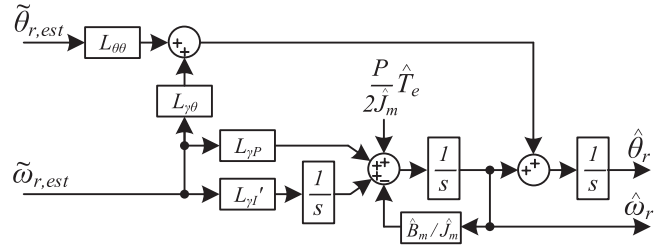

Fig. 6. Position and speed estimator using speed error in [27].

errors in Fig. 3 because they use only one input $\tilde{\theta}_{r,\rm est}$. However, in the proposed method, $\tilde{\omega}_{r,\rm est}$ is extracted as well as $\tilde{\theta}_{r,\rm est}$ simultaneously and independently. Therefore, in this paper, a new position and speed estimator that is compatible with the estimated errors in Fig. 3 is devised. For the design of this estimator, the state equation of (7) is applied, and its structure is shown in Fig. 5. In this figure, $L'_{\gamma I}$ indicates $-PL_{\gamma I}/2\hat{J}_m$

$$\frac{d}{dt}\mathbf{x} = \mathbf{A}\mathbf{x} + \mathbf{B}\hat{T}_e + \mathbf{L}\begin{bmatrix}\tilde{\theta}_r\\ \tilde{\omega}_r\end{bmatrix} \tag{7}$$

$$\text{where } \mathbf{A} = \begin{bmatrix}0 & 1 & 0 & L_{\gamma\theta}\\ 0 & -\frac{\hat{B}}{\hat{J}_m} & -\frac{P}{2\hat{J}_m} & L_{\gamma P}\\ 0 & 0 & 0 & L_{\gamma I}\\ 0 & 0 & 0 & 0\end{bmatrix} \mathbf{L} = \begin{bmatrix}L_{\theta\theta} & L_{\gamma\theta}\\ L_{\theta P} & L_{\gamma P}\\ L_{\theta I} & L_{\gamma I}\\ L_{\theta\gamma} & 0\end{bmatrix}$$

$\mathbf{x} = [\hat{\theta}_r\ \hat{\omega}_r\ \hat{T}_{\rm load}\ \gamma_{\rm in}{}']^T$ and $\mathbf{B} = [0\ {\rm P}/2\hat{J}_m\ 0\ 0]^T$. As shown in (7) and in Fig. 5, the input stage of the estimator has been modified from the estimator in Fig. 6 [27]. The position and speed estimator in Fig. 6 is based on a lower order state equation than (7), i.e., $\mathbf{x} = [\hat{\theta}_r\ \hat{\omega}_r\ \hat{T}_{\rm load}]^T$. Therefore, the position and speed are adjusted in the direction such that $\tilde{\omega}_{r,\rm est}$ is nullified rather than $\tilde{\theta}_{r,\rm est}$, as shown in Fig. 6. In case where an error arises in $\tilde{\omega}_{r,\rm est}$, however the estimator in Fig. 6 results in a steady-state speed error. Moreover, gain setting becomes difficult because the position estimation error is influenced by $L_{\theta\theta}$ and by parameter errors. Therefore, in the proposed estimator in Fig. 5, the additional state variable $\gamma'_{\rm in}$ has been added from Fig. 6. Even if one pole to be placed has been increased, the position and speed can now be estimated in the direction such that $\tilde{\theta}_{r,\rm est}$ is nullified, meaning that the steady-state speed error can be eliminated and the steady-state position error becomes independent of the gain as well.

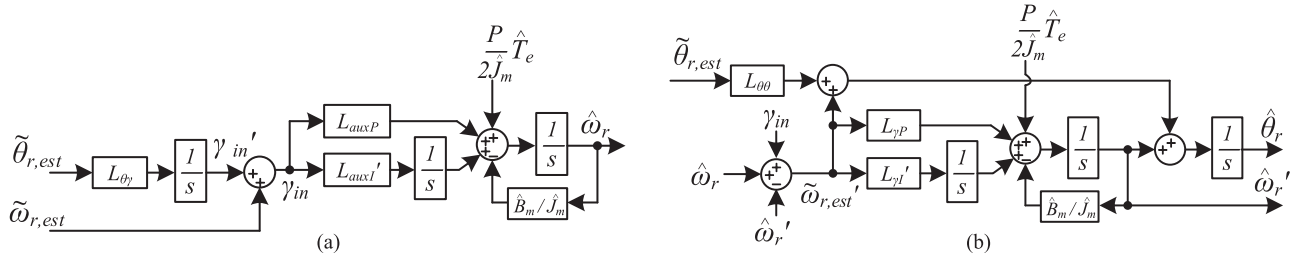

Fig. 7. Modified position and speed estimator including an auxiliary speed estimator. (a) Auxiliary speed estimator. (b) Modified position estimator.

In determination of the gains in (7), it is assumed that $\tilde{\theta}_{r,\mathrm{est}}$ and $\tilde{\omega}_{r,\mathrm{est}}$ are extracted without error, that is, $\tilde{\theta}_{r,\mathrm{est}}$ and $\tilde{\omega}_{r,\mathrm{est}}$ are identical to $\theta_r - \hat{\theta}_r$ and $\omega_r - \hat{\omega}_r$, respectively. The transfer functions from θ_r to $\hat{\theta}_r$ and from ω_r to $\hat{\omega}_r$ can then be derived by the following equation:

$$\begin{aligned}\hat{\theta}_r &= H_{\theta\theta}(s)\,\theta_r + H_{\theta T}(s)\,\Delta T \\ \hat{\omega}_r &= H_{\omega\omega}(s)\,\omega_r + H_{\omega T}(s)\,\Delta T\end{aligned} \tag{8}$$

where ΔT is defined as the disturbance torque, which is the difference between the feedforward torque $\hat{T}_e$ and the net torque applied to the motor, i.e., $T_e - T_{\mathrm{load}}$. $H_{\theta\theta}$, $H_{\theta T}$, $H_{\omega\omega}$, and $H_{\omega T}$ are described in detail in the appendix. It should be noted that $L_{\gamma\theta} = 1$ can eliminate the effect of ΔT on $\hat{\theta}_r$ from $H_{\theta T}$. Therefore, by introducing $\tilde{\omega}_{r,\mathrm{est}}$ into the estimator, it is expected that robustness of the position estimation to load torque variations can be enhanced. In addition, in (17) in the appendix, it should also be noted that the two gains of $\tilde{\theta}_r$ in the first column in (7), i.e., $L_{\theta P}$ and $L'_{\theta I}$, are disabled by $L_{\gamma\theta} = 1$, where $L'_{\theta I}$ is defined as $-PL_{\theta I}/2\hat{J}_m$. This is already reflected in Fig. 5.

Additionally, even if it appears that (8) is a second-order system, it becomes a fourth-order system if there is an error in $\tilde{\theta}_{r,\mathrm{est}}$ or $\tilde{\omega}_{r,\mathrm{est}}$. Therefore, all gains should be set and can be determined by the multiplication of two characteristic equations of the general second-order system in the following equation:

$$\begin{aligned}s^2 + 2\zeta_{n,1}\omega_{n,1}s + {\omega_{n,1}}^2 &= s^2 + \left(\frac{\hat{B}_m}{\hat{J}_m} + L_{\gamma P}\right)s + {L_{\gamma I}}' \\ s^2 + 2\zeta_{n,2}\omega_{n,2}s + {\omega_{n,2}}^2 &= s^2 + L_{\theta\theta}s + L_{\theta\gamma}.\end{aligned} \tag{9}$$

Using the relationship in (9), four gains in addition to $L_{\gamma\theta} = 1$ can be determined in accordance with the desirable natural frequency ω_n and damping factor ζ_n.

B. Auxiliary Speed Estimator

Although the response of $\hat{\theta}_r$ to ΔT can be enhanced by the estimator in Fig. 5, that of $\hat{\omega}_r$ is still affected by ΔT. Even if the increased gains would naturally reduce the effects, the gains cannot be increased above certain limit in some cases, such as when large harmonic components exist in the back-EMF voltage and inductances [30] or in the case of fixed gains for a wide speed range. Therefore, in this paper, apart from the position estimator, an auxiliary speed estimator is also proposed, as shown in Fig. 7(a). Moreover, the original estimator in Fig. 5 is changed to Fig. 7(b) with a modified input stage. The modified estimator operates together with the auxiliary estimator in Fig. 7(a), which is based on the state equation in the following equation:

$$\begin{aligned}\frac{d}{dt}\begin{bmatrix}\hat{\omega}_r \\ \hat{T}_L\end{bmatrix} &= \begin{bmatrix}-\dfrac{\hat{B}_m}{\hat{J}_m} & -\dfrac{P}{2\hat{J}_m} \\ 0 & 0\end{bmatrix}\begin{bmatrix}\hat{\omega}_r \\ \hat{T}_L\end{bmatrix} \\ &\quad + \begin{bmatrix}\dfrac{P}{2\hat{J}_m} \\ 0\end{bmatrix}\hat{T}_e + \begin{bmatrix}L_{\mathrm{aux}P} \\ L_{\mathrm{aux}I}\end{bmatrix}\left({\gamma_{\mathrm{in}}}' + \tilde{\omega}_r\right).\end{aligned} \tag{10}$$

The auxiliary estimator has a structure similar to that of the original estimator, but it is entirely separate from the position estimator in Fig. 7(b). With the proposed auxiliary estimator, the dynamics of the speed estimation can be enhanced while maintaining the characteristics of the position estimation process.

Similar to the gain setting method in (9), $L_{\mathrm{aux}P}$ and $L'_{\mathrm{aux}I}$ can be determined by the second-order transfer function in the following equation:

$$\hat{\omega}_r = \frac{\left\{\frac{J_m}{\hat{J}_m}s^2 + \left(L_{\mathrm{aux}P} + \frac{B_m}{\hat{J}_m}\right)s + {L_{\mathrm{aux}I}}'\right\}\gamma_{\mathrm{in}} + \frac{P}{2\hat{J}_m}s\Delta T}{s^2 + \left(L_{\mathrm{aux}P} + \frac{\hat{B}_m}{\hat{J}_m}\right)s + {L_{\mathrm{aux}I}}'} \tag{11}$$

where $L'_{\mathrm{aux}I}$ is defined as $-PL_{\mathrm{aux}I}/2\hat{J}_m$. Also, in (11), $\tilde{\omega}_{r,\mathrm{est}} = \tilde{\omega}_r$ and ${\gamma_{\mathrm{in}}}' \approx 0$ are assumed because ${\gamma'_{\mathrm{in}}}$ varies slowly compared to $\tilde{\omega}_{r,\mathrm{est}}$ and the steady-state value is zero. For the auxiliary speed estimator to reduce the effects of ΔT on $\hat{\omega}_r$ or enhance the dynamics, it should have a higher bandwidth than that of the original estimator. In this way, more robust speed-estimation performance can be achieved while minimizing the effects of noise on $\hat{\theta}_r$.

On the other hand, for the design of the original estimator to remain valid, the speed error input $\tilde{\omega}'_{r,\mathrm{est}}$ to the estimator in Fig. 7(b) should be the difference between the actual speed ω_r and the unused state variable $\hat{\omega}'_r$ in Fig. 7(b). For calculation of $\omega_r - \hat{\omega}'_r$, the following calculation method can be used:

$$\begin{aligned}\tilde{\omega}'_{r,\mathrm{est}} &= \gamma_{\mathrm{in}} + \hat{\omega}_r - \hat{\omega}'_r \\ &\approx (\omega_r - \hat{\omega}_r) + \hat{\omega}_r - \hat{\omega}'_r \approx \omega_r - \hat{\omega}'_r.\end{aligned} \tag{12}$$

In (12), γ_{in} can be approximated as $\omega_r - \hat{\omega}_r$ if parameter errors and voltage distortion are not considered. Therefore, using the input stage in Fig. 7(b), the auxiliary speed estimator can be linked to the original estimator without any effects on the characteristics of the original estimator.

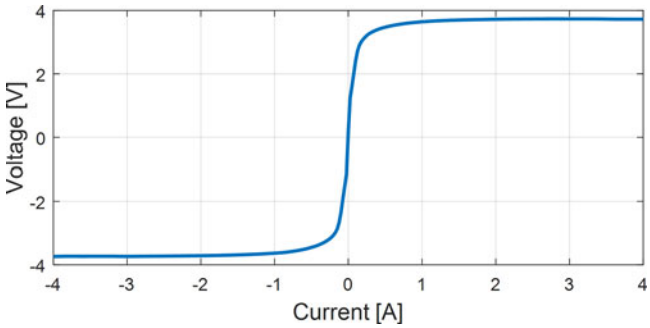

Fig. 8. Voltage distortion of the prototype inverter by the phase current.

V. Experimental Results

The test setup used to evaluate the proposed sensorless method and the estimator was constructed based on a TMS320F28377 digital signal processor (DSP). The power device used in the prototype inverter was a Mitsubishi PSS10S51F6 IPM. Also, $f_{sw} = 10$ kHz, $f_{\rm samp} = 20$ kHz, $V_{\rm dc} = 311$ V, and $T_{\rm dead}$ was set to 1 μs to minimize the voltage distortion by the inverter. In addition to the small dead time, the compensation voltage in Fig. 8 was superimposed onto the output voltages of the controller by each phase current [37]. The target motor under test is an IPMSM of the type used in servo applications, the parameters of which are specified in Table I. In addition, in the experimental setup, a motor–generator set was established to emulate the load.

In the model-based sensorless method, the accuracy of the parameters is directly related to the estimation performance. Regarding L_{qs} in the test motor, it is nearly constant if T_e is in the range of 0.3–0.7 p.u. Therefore, for convenience, the experiments are designed in this range.

For the verification of the proposed estimation method and the estimators, the following experiments are designed, indicating that the estimated errors, i.e., $\tilde{\theta}_{r,\rm est}$ and $\tilde{\omega}_{r,\rm est}$, are in satisfactory agreement with the actual errors and that the sensorless control performance can be significantly enhanced by the proposed methods in the current and speed control modes.

A. Rapid Speed Variation (20000 r/min /s) in the Current Control Mode

In Figs. 9 and 10, the performances of position and speed estimations are presented when the test motor is in the current control mode ($T_e^* = 0.5$ p.u.) and with rapid changes in the operating speed of the load machine. The rotating speed was varied by the load machine from 2000 to 2500 r/min, and back to 2000 r/min again in Fig. 9. It was also varied from 500 to 1000 and then to 500 r/min again in Fig. 10 at a rate of 20000 r/min/s.

First, from the second and third rows in Figs. 9 and 10, the proposed estimation method by (6) can be verified by comparing $\tilde{\theta}_{r,\rm est}$ and $\tilde{\omega}_{r,\rm est}$ with the actual errors, i.e., $\tilde{\theta}_r$ and $\tilde{\omega}_r$, from a position sensor. In this experiment, the test motor was operated without the aid of the position sensor, which was used only for observing the actual errors. From the figure, it can be seen that $\tilde{\theta}_{r,\rm est}$ and $\tilde{\omega}_{r,\rm est}$ are accurately estimated even during the highly dynamic operation, although they are delayed by approximately 10 ms in the worst case at 500 r/min, as shown in Fig. 10, which is inevitable because the effect of the ignored term in (6) increases at a low speed. Therefore, considering the experimental results, a more suitable sensorless control method is preferred, such as a high-frequency signal injection method at speeds of less than 500 r/min. However, at speeds higher than or equal to 500 r/min, the assumption in (6) is reasonable and the estimated errors can be used as input for the proposed estimators in Figs. 5 and 7.

In Figs. 9 and 10, the estimation and current control performances of the proposed methods are compared with those by the conventional method applying the position and speed estimator and the estimation method shown in Figs. 1 and 2, respectively. In this experiment, the low-pass filter in Fig. 2(a) has been removed such that only the dynamics of the estimator in Fig. 1 is taken into account. In Figs. 9 and 10, the experimental results for the conventional method are presented in the first row and the results for the proposed methods without and with the auxiliary estimator are shown in the second and third rows, respectively. Even when the dominant pole of the estimators has been set equal to 4 Hz in both cases, which is the edge of the stable response for the conventional method at 500 r/min, it is clear that the estimation performances in Figs. 9(c) and 10(c) have been enhanced remarkably in comparison with the conventional method. In this experiment, the poles are set as follows: $p_n = 14$ Hz, $\omega_n = 4$ Hz, and $\zeta_n = 1.1$ for the characteristic equation of the conventional estimator, i.e., $(s+p_n)(s^2+2\zeta_n\omega_n s+\omega_n^2)=0$; $\omega_{n,1} = 4$ Hz, $\zeta_{n,1} = 1.1$, $\omega_{n,2} = 4$ Hz, and $\zeta_{n,2} = 2.3$ for the proposed estimator in (9); $\omega_{n,\rm aux} = 5$ Hz, $\zeta_{n,\rm aux} = 1.4$ for the auxiliary estimator. In the gain-setting procedure, L_1 in Fig. 1 and $L_{\theta\theta}$ in Figs. 5 and 7(b) have identical values, adapting $\zeta_{n,2}$ for the same effect of the feedforward terms. Also, in the experiments, the low gains selected for low-speed operation so as to reject harmonic disturbances are assumed to be held equal except for $\omega_{n,\rm aux} = 7$ Hz at high speeds to show that the performance can be enhanced even more.

In Fig. 10(a), the position error exceeds the stability limit of 90 °E, and it can be seen that the applied load torque changes abruptly to regulate the speed. Meanwhile, in Figs. 9(b) and (c) and 10(b) and (c), the maximum position error is less than 10 °E and 20 °E, respectively, even under transient conditions. Even if $H_{\theta T}$ in (17) is nullified by setting $L_{\gamma\theta}$ equal to 1, the actual experiment returned a position estimation error. It is likely to have been induced from the errors in the parameters in (6). Specifically, the errors in (6) undermine the assumptions in (8), i.e., $\tilde{\theta}_{r,\rm est} = \theta_r - \hat{\theta}_r$ and $\tilde{\omega}_{r,\rm est} = \omega_r - \hat{\omega}_r$.

Figs. 9(c) and 10(c), where the auxiliary speed estimator is included, show that response time has been reduced by more than 100 ms in both speed cases, with a reduction in the maximum speed error by more than 30% in the high-speed case as compared to the outcomes in Figs. 9(a) and (b) and 10(a) and (b). The speed response can be more clearly compared by examining Figs. 9(d) and 10(d). From these figures, it is clear that the estimated speed as well as the estimated position track the actual values much more rapidly under highly dynamic operations, even if the convergence has not been shortened without the auxiliary estimator. In Figs. 9(a) and (b) and 10(a) and (b),

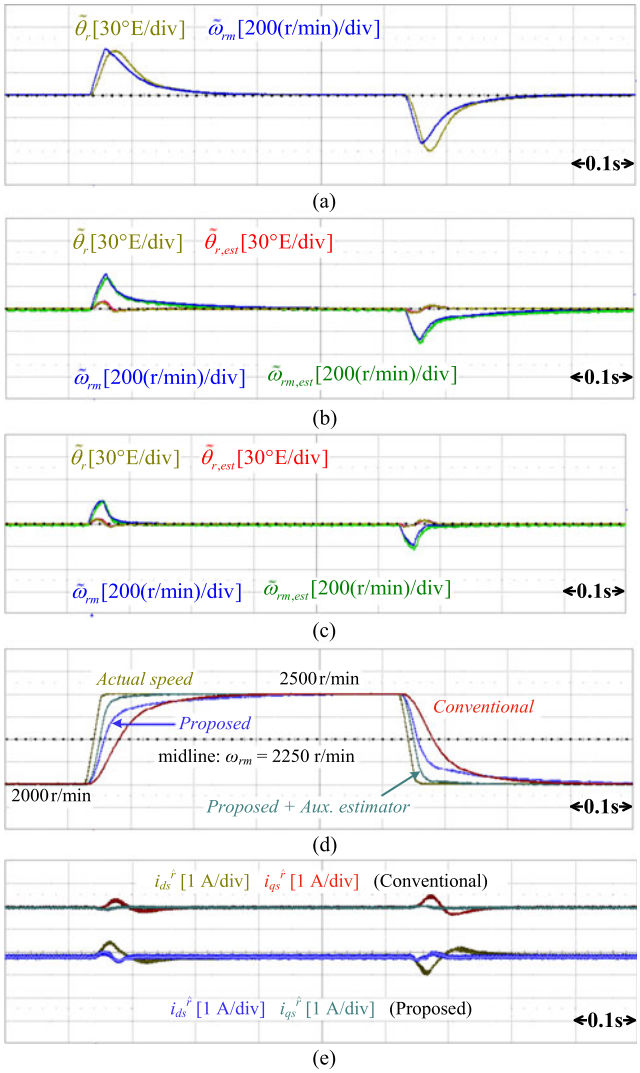

Fig. 9. Estimation performance during speed variation (2000 ↔ 2500 r/min). (a) Conventional method. (b) Proposed method without an auxiliary speed estimator. (c) Proposed method with an auxiliary speed estimator. (d) Comparison of the estimated speed. (e) Comparison of the current response.

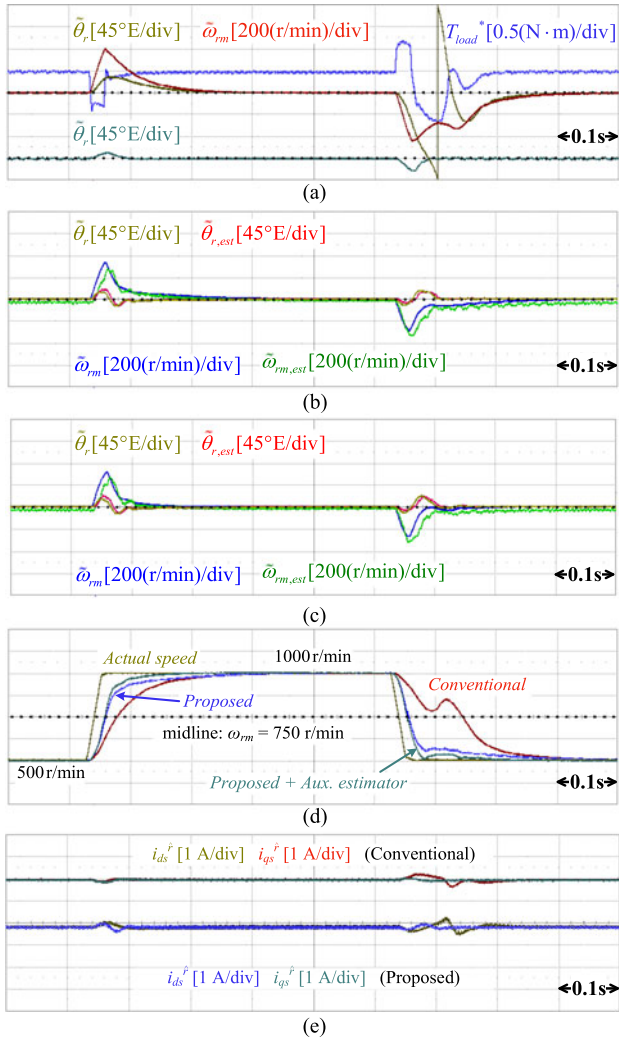

Fig. 10. Estimation performance during speed variation (500 ↔ 1000 r/min). (a) Conventional method. (b) Proposed method without an auxiliary speed estimator. (c) Proposed method with an auxiliary speed estimator. (d) Comparison of the estimated speed. (e) Comparison of the current response.

the convergence time of the overall estimation is approximately 250 ms. However, with regard to the position estimation, the convergence time has been reduced by more than 70% in both speed cases by applying the proposed methods.

In Figs. 9(e) and 10(e), the current response is presented. In these figures, the conventional and the proposed methods without the auxiliary estimator are compared. As noted earlier, because the current reference is determined by the fixed torque reference ($T_e^* = 0.5$ p.u.), the d and q axes currents should maintain their values against external variations. In Fig. 9(e), where the operating speed is sufficiently high and the position estimation error is considerably reduced, the performance is clearly enhanced compared to that in Fig. 10(e). Meanwhile, at lower speed where the position estimation is not remarkably reduced, the average variation shows no improvements from the conventional case despite the fact that it is much better during the second transient, where the conventional method loses the tracking.

At the bottom of Fig. 10(a), an additional trace for the conventional method is plotted, where higher gains were assessed for a similar magnitude of the position error with the proposed methods. For this waveform, the poles are placed at $p_n = 15$ Hz, $\omega_n = 10$ Hz, and $\zeta_n = 1.1$, and it should be noted that the dominant pole is more than two times that in the original case. Naturally, it would be more sensitive to external noise and harmonic components.

B. Abrupt Load Torque Disturbance (10 p.u./s) in the Speed Control Mode

In this experiment, robustness is tested in the speed control mode when the load torque $T_{\rm load}$ is changed from 0.3 to 0.7 p.u. and then back to 0.3 p.u. at a rate of 10 p.u./s, as shown in Fig. 11(d). The operating speed is regulated by the test motor, which operates at 2000 r/min in Fig. 11 and at 500 r/min in Fig. 12.

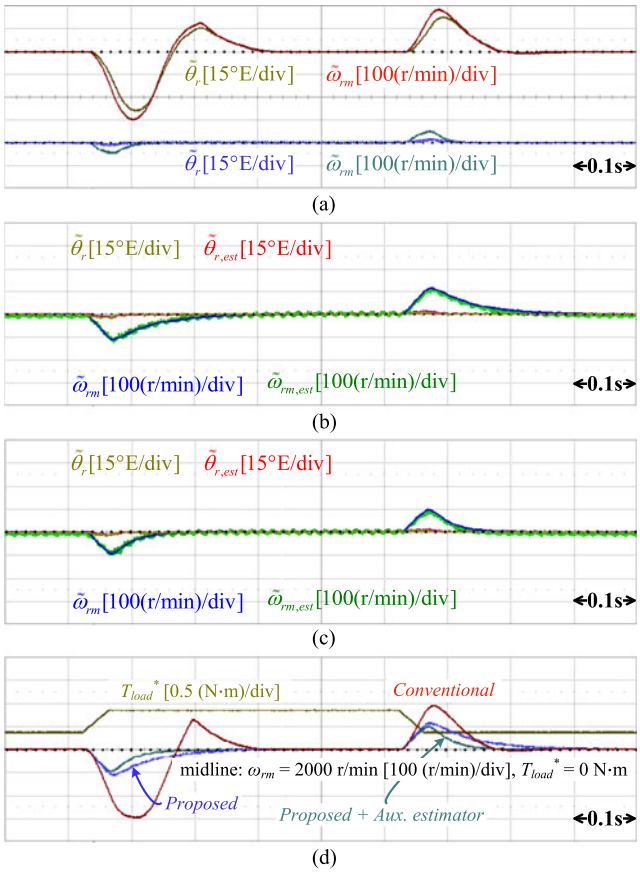

Fig. 11. Estimation performance during load torque variation (0.3 ↔ 0.7 p.u., speed reference: 2000 r/min). (a) Conventional method. (b) Proposed method without an auxiliary speed estimator. (c) Proposed method with an auxiliary speed estimator. (d) Comparison of the actual speeds.

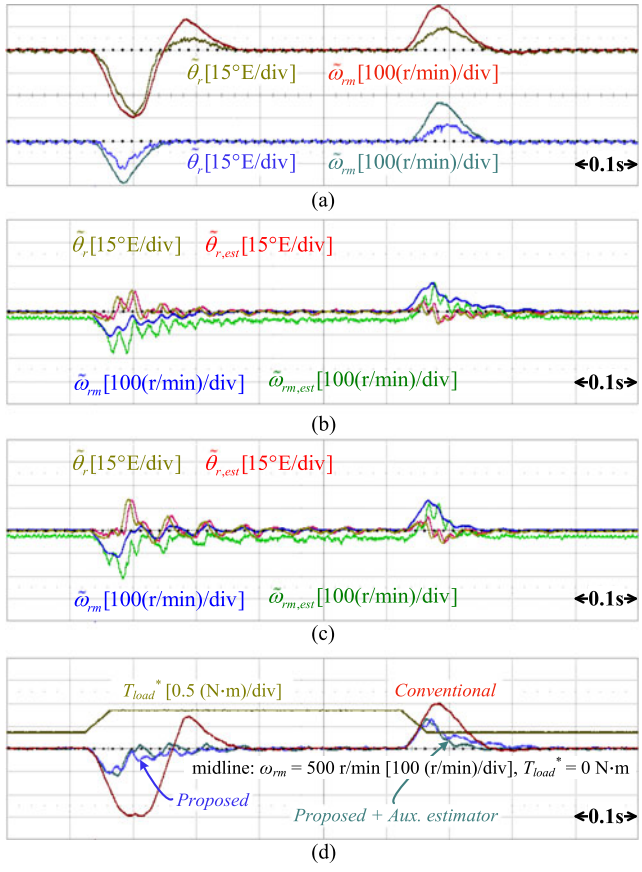

Fig. 12. Estimation performance during load torque variation (0.3 ↔ 0.7 p.u., speed reference: 500 r/min). (a) Conventional method. (b) Proposed method without an auxiliary speed estimator. (c) Proposed method with an auxiliary speed estimator. (d) Comparison of the actual speeds.

Similar to the first experiment, the gains were set as the edge for the conventional method to keep the speed at 500 r/min under a severe load torque transient. That is, $p_n = 14$ Hz, $\omega_n = 5$ Hz, and $\zeta_n = 1.1$ were used for the conventional estimator; $\omega_{n,1} = 5$ Hz, $\zeta_{n,1} = 1.1$, $\omega_{n,2} = 5$ Hz, and $\zeta_{n,2} = 2.1$ for the proposed estimator; and $\omega_{n,\mathrm{aux}} = 6$ Hz and $\zeta_{n,\mathrm{aux}} = 1.1$ for the auxiliary estimator at 500 r/min and $\omega_{n,\mathrm{aux}} = 7$ Hz at 2000 r/min. The bandwidth of the speed controller was set to 35 Hz.

Figs. 11 and 12 show the position and speed estimation performances of the conventional and proposed methods when they are exposed to load variations. In Fig. 11, where the test motor regulates the speed as 2000 r/min, it can be observed that while the maximum position error in Fig. 11(a) is about 35 °E during the first transient, the errors in Fig. 11(b) and (c) are less than 3 °E, which is less than one tenth of that in the first case. Similarly, the maximum speed error of the conventional method is 300 r/min during the first transient. However, it can be seen that the speed error was reduced to about 100 r/min when applying the proposed methods. In Fig. 11(d), where the actual speeds of each method are compared, it is shown that not only has the magnitude of the errors been decreased but that the convergence time has also been reduced by 100 ms during the first transient when the auxiliary estimator is employed. Therefore, it can be concluded that the robustness against load variations has been remarkably enhanced by the proposed methods.

In Fig. 12, where the test motor regulates the speed as 500 r/min, it can be observed that while the maximum position and speed errors during the first transient are reduced by half and by 60%, respectively, when using the proposed methods, the response becomes oscillatory. Regarding the oscillatory response, it was verified by the simulation including the inverter model that the oscillatory response comes from imperfect compensation of the voltage distortion in Fig. 8, as the effect of voltage error increases at lower speeds. In Fig. 12(b) and (c), the voltage error is represented as the estimated speed error with a dc value. Because the proposed methods estimate the position and speed by nullifying the estimated position error, the estimated speed error can have a dc value if the parameter information or voltage compensation is inaccurate. Therefore, even if the compensation of the voltage distortion is not the focus in this paper, a more appropriate compensation method would be preferable to eliminate the oscillation, especially in the low-speed control mode. Despite the harmonic oscillation, however, Fig. 12 indicates that the low-speed response can also be more robust against load torque transients when using the proposed methods, reducing the possibility of the failure of the sensorless control.

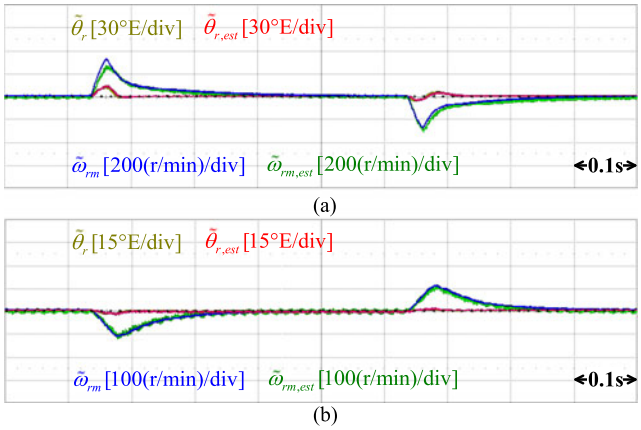

Fig. 13. Estimation performances from previous research [27]. (a) During speed variation (2000 ↔ 2500 r/min). (b) During load torque variation (0.3 ↔ 0.7 p.u., speed reference: 2000 r/min).

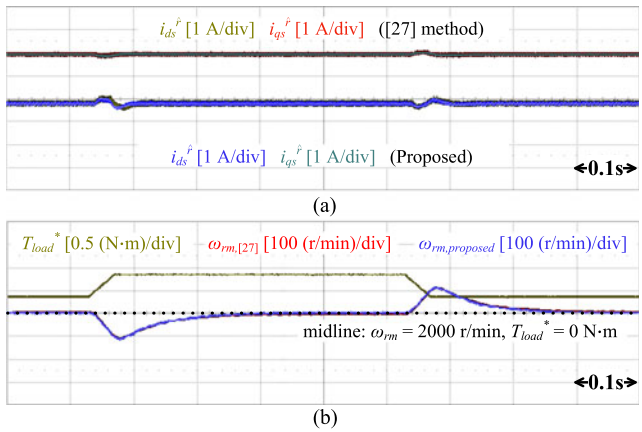

Fig. 14. Comparison of performances with previous research. (a) Current response against speed variation. (b) Speed response against load torque variation.

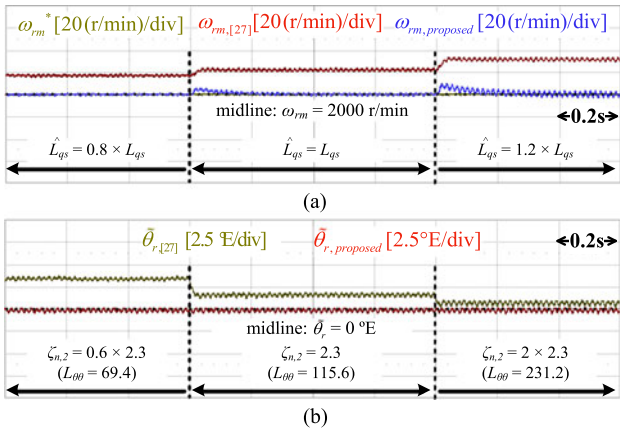

Fig. 15. Comparison of estimation performances under nonideal conditions. (a) Variation of estimated L_{qs}. (b) Variation of $L_{\theta\theta}$.

At the bottom of Figs. 11(a) and 12(a), an additional trace for the conventional method is shown. In these waveforms, in the same way of Fig. 10(a), higher gains were assessed for the position estimation performance similar to that of the proposed methods. Here, the poles are placed at $p_n = 28$ Hz, $\omega_n = 14$ Hz, and $\zeta_n = 1.1$ in Fig. 11(a) and at $p_n = 14$ Hz and $\omega_n = 6$ Hz with the same value of ζ_n in Fig. 12(a). Fig. 11(a) indicates that the position estimation error is comparable to the errors in Fig. 11(b) and (c) with the reduced speed error and convergence time although the dominant pole in this case is nearly three times larger than in the first case. Meanwhile, in the low-speed case, a small increase of the gain resulted in a reduction of the position error by 50%. However, the increased load began to bring about mechanical vibration at this or higher gains. Therefore, these results indicate that the position estimation performance of the conventional method is very sensitive to the gain and that the possible range of the gains is quite limited in the low-speed control mode.

C. Comparison With the Previous Research [27]

Because the proposed method is an improvement over an earlier method [27], comparison results from the previous study [27] are provided in addition to the results given in Figs. 9–12.

First, Fig. 13 shows the estimation performance from the earlier work [27] in terms of speed variation and load torque variation, which corresponds to Figs. 9(b) and Fig. 11(b), respectively. Here, all gains are equal to those of the corresponding experimental conditions. In these figures, it can be observed that the responses by two methods are nearly identical during a rapid transient, indicating that newly the designed state $\gamma_{\text{in}}{}'$ in (7) and Fig. 5 rarely affects the dynamic characteristics as expected.

Fig. 14 shows similar results in the current and speed control modes. In Fig. 14(a), the current responses of the method under comparison [27] and of the proposed method without an auxiliary estimator are overlapped. The overlapped speed responses are also given in Fig. 14(b). From these figures, it can be concluded that the dynamic characteristics in two methods are identical.

Meanwhile, in Fig. 15, practical issues are considered. As aforementioned, the reasons for including the state variable, γ'_{in}, contrast to the earlier study [27], where no γ'_{in} is, are because: 1) the steady-state speed error can be eliminated, and 2) the steady-state position error becomes independent of the gain. Fig. 15(a) illustrates the first reason. In this experiment, the test motor operates in the speed control mode with a speed reference of 2000 r/min. In addition, $\hat{L}_{qs}$ was intentionally varied from $0.8\,L_{qs}$ to L_{qs} at 0.6 s, and then to $1.2L_{qs}$ at 1.4 s. In Fig. 15(a), it can be observed that the estimated speed by earlier method [27] differs from the reference, whereas the proposed method tracks the reference well. Moreover, when $\hat{L}_{qs} = L_{qs}$, it is clear that there is a speed error in the previous method even if no intentional parameter error existed and the compensation voltage in Fig. 8 was applied, which means that $\tilde{\omega}_{r,\text{est}}$ is not entirely accurate. However, accurate speed control is possible with the proposed method regardless of the position error from $\hat{L}_{qs}$.

On the other hand, Fig. 15(b) shows the effect of $L_{\theta\theta}$. In Fig. 15(b), the test motor is controlled in the current control mode with $T_e^* = 0.5$ p.u., and $L_{\theta\theta}$ was varied from 60% of the

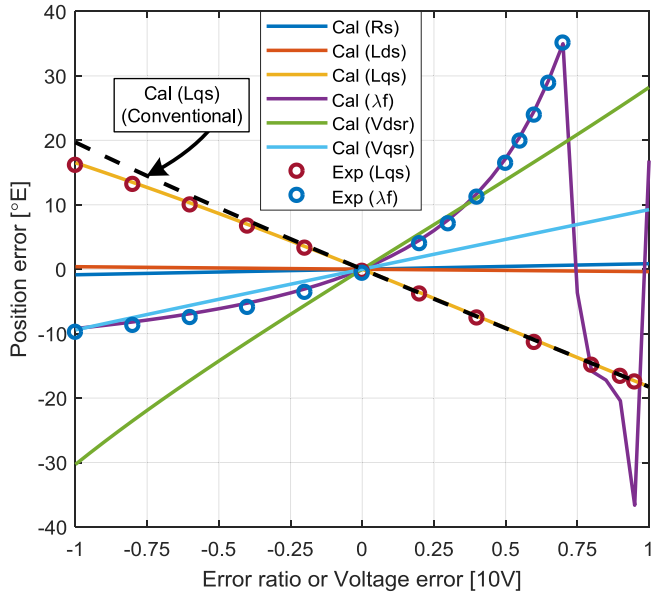

Fig. 16. Calculated and experimental results for the position estimation error induced by parameter errors and voltage distortion.

original value to 100% at 0.6 s, and then to 200% at 1.4 s. In this figure, it can be observed that the position error is affected by the variation of $L_{\theta\theta}$, as $\tilde{\omega}_{r,\mathrm{est}}$ is nullified by the estimator in Fig. 6, rather than $\tilde{\theta}_{r,\mathrm{est}}$, while the proposed method is not affected by $L_{\theta\theta}$ at all.

D. Effects of Parameter Errors on the Steady-State Position Error

Theoretically, the resulting position error can be calculated by substituting $\tilde{\theta}_{r,\mathrm{est}}$ in (6) with 0, from which (13) can be deduced as follows:

$$\begin{bmatrix} -\omega_{q,\mathrm{est}} \\ \omega_{d,\mathrm{est}} \end{bmatrix}^T \left(\begin{bmatrix} \tilde{v}_{ds}^{\hat{r}} \\ \tilde{v}_{qs}^{\hat{r}} \end{bmatrix} + \begin{bmatrix} \tilde{R}_s & -\omega_r \tilde{L}_{qs} \\ \omega_r \tilde{L}_{ds} & \tilde{R}_s \end{bmatrix} \begin{bmatrix} i_{ds}^{\hat{r}} \\ i_{qs}^{\hat{r}} \end{bmatrix} + \begin{bmatrix} 0 \\ \omega_r \tilde{\lambda}_f \end{bmatrix} + \omega_r \lambda_f \begin{bmatrix} -\sin\tilde{\theta}_r \\ \left(\cos\tilde{\theta}_r - 1\right) \end{bmatrix} + \omega_r \Delta L_s \begin{bmatrix} -\sin 2\tilde{\theta}_r & \cos 2\tilde{\theta}_r - 1 \\ \cos 2\tilde{\theta}_r - 1 & \sin 2\tilde{\theta}_r \end{bmatrix} \begin{bmatrix} i_{ds}^{\hat{r}} \\ i_{qs}^{\hat{r}} \end{bmatrix} \right) = 0. \tag{13}$$

In (13), $\tilde{v}_{dqs}^{\hat{r}}$, $\tilde{R}_s$, $\tilde{L}_{ds}$, $\tilde{L}_{qs}$, and $\tilde{\lambda}_f$ indicate the voltage error on the d and q axes and the parameter errors of the resistance, inductances, and back-EMF constant, respectively. Using (13), the position estimation error induced from each element was calculated. Calculated results are plotted in Fig. 16, where the error ratio is defined as the error divided by the actual value. In the calculation, 50% load and 1000 r/min conditions were assumed, and because the relationship in (13) is not linear or analytic, the estimation error was obtained recursively with an initial value of $\tilde{\theta}_r = 0$. From the figure, it can be observed that the effects of $\tilde{L}_{qs}$, $\tilde{\lambda}_f$, and $\tilde{v}_{ds}^{\hat{r}}$ on the position error are significant. Specifically, the estimation error increases exponentially as $\tilde{\lambda}_f$ increases in the positive direction, whereas the errors from others are linear. Additionally, in Fig. 16, the position estimation error from L_{qs}, when the conventional method in Figs. 1 and 2 is applied, has been calculated [16] and shown for comparison, as denoted by the black dotted line. As shown in Fig. 16, the effects of L_{qs} are similar in the two methods. Meanwhile, λ_f is irrelevant with regard to the position estimation when using the conventional method with EEMF, as the main error signal $e_{ds,\mathrm{est}}^{\hat{r}}$ is independent of λ_f, as shown in (14), while the proposed method is significantly affected by the error of λ_f

$$e_{ds,\mathrm{est}}^{\hat{r}} = v_{ds}^{\hat{r}*} - \hat{R}_s i_{ds}^{\hat{r}} + \hat{\omega}_r \hat{L}_{qs} i_{qs}^{\hat{r}} \propto \tilde{\theta}_r. \tag{14}$$

Therefore, accurate estimations of the parameters including λ_f are the utmost important when using the proposed methods.

To verify the calculation, the estimated parameters were intentionally varied in the experiment, and the resulting position errors were then measured and the results are overlapped onto Fig. 16. In the experiment, $\tilde{L}_{qs}$ and $\tilde{\lambda}_f$ among the main sources of error were changed because the voltage error is difficult to define due to voltage distortion by the inverter. As shown in Fig. 16, the position errors from the experiment are in good agreement with the calculated results. From this comparison, it has been verified that the position estimation error in a steady state is only affected by $\tilde{\theta}_{r,\mathrm{est}}$ and that $\tilde{\omega}_{r,\mathrm{est}}$ simply assists with the estimation to achieve enhanced robustness.

VI. Conclusion

In this paper, a new estimation method for position and speed errors and compatible position and speed estimators were proposed and the effects of parameter errors on the position estimation error were analyzed. In the proposed method, the speed error and the position error were extracted by splitting the actual speed in the voltage equation into the estimated and error terms. In addition, the position and speed estimator using the estimated errors were designed to nullify the speed error in a steady state, and a guideline by which to set the gains of the estimator was described. Additionally, an auxiliary speed estimator was devised and combined with the first estimator to enhance the robustness and the speed-estimation capabilities by the proposed methods.

All of the proposed methods and the analyses were verified by experiments. The experimental results demonstrated the effectiveness of the proposed methods under highly dynamic operating conditions, such as speed variation at a rate of 20000 r/min/s in the current control mode and load disturbance at a rate of 10 p.u./s in the speed control mode. With the proposed methods, maximum position errors were conspicuously reduced by 70% during speed transient and by 50% under load disturbance with identical dominant-pole placements, verifying the enhanced tracking capability and robustness offered by these novel methods.

Appendix

Here, the long and complex equations that cannot be placed in the main text are presented as follows.

$$\begin{bmatrix} v_{ds}^{\hat{r}} \\ v_{qs}^{\hat{r}} \end{bmatrix} = R_s \begin{bmatrix} i_{ds}^{\hat{r}} \\ i_{qs}^{\hat{r}} \end{bmatrix} + \begin{bmatrix} L_{ds}\cos^2\tilde{\theta}_r + L_{qs}\sin^2\tilde{\theta}_r & (L_{ds}-L_{qs})\sin\tilde{\theta}_r\cos\tilde{\theta}_r \\ (L_{ds}-L_{qs})\sin\tilde{\theta}_r\cos\tilde{\theta}_r & L_{ds}\sin^2\tilde{\theta}_r + L_{qs}\cos^2\tilde{\theta}_r \end{bmatrix} p \begin{bmatrix} i_{ds}^{\hat{r}} \\ i_{qs}^{\hat{r}} \end{bmatrix} + \omega_r \lambda_f \begin{bmatrix} -\sin\tilde{\theta}_r \\ \cos\tilde{\theta}_r \end{bmatrix}$$

$$+ p\tilde{\theta}_r \begin{bmatrix} -(L_{ds}-L_{qs})\sin\tilde{\theta}_r\cos\tilde{\theta}_r & L_{ds}\cos^2\tilde{\theta}_r + L_{qs}\sin^2\tilde{\theta}_r \\ -L_{ds}\sin^2\tilde{\theta}_r - L_{qs}\cos^2\tilde{\theta}_r & (L_{ds}-L_{qs})\sin\tilde{\theta}_r\cos\tilde{\theta}_r \end{bmatrix} \begin{bmatrix} i_{ds}^{\hat{r}} \\ i_{qs}^{\hat{r}} \end{bmatrix}$$

$$+ \omega_r \begin{bmatrix} -(L_{ds}-L_{qs})\sin\tilde{\theta}_r\cos\tilde{\theta}_r & -L_{ds}\sin^2\tilde{\theta}_r - L_{qs}\cos^2\tilde{\theta}_r \\ L_{ds}\cos^2\tilde{\theta}_r + L_{qs}\sin^2\tilde{\theta}_r & (L_{ds}-L_{qs})\sin\tilde{\theta}_r\cos\tilde{\theta}_r \end{bmatrix} \begin{bmatrix} i_{ds}^{\hat{r}} \\ i_{qs}^{\hat{r}} \end{bmatrix} \tag{15}$$

$$\begin{bmatrix} v_{ds}^{\hat{r}} \\ v_{qs}^{\hat{r}} \end{bmatrix} = R_s \begin{bmatrix} i_{ds}^{\hat{r}} \\ i_{qs}^{\hat{r}} \end{bmatrix} + \begin{bmatrix} L_{ds} & 0 \\ 0 & L_{qs} \end{bmatrix} p \begin{bmatrix} i_{ds}^{\hat{r}} \\ i_{qs}^{\hat{r}} \end{bmatrix} + \hat{\omega}_r \begin{bmatrix} 0 & -L_{qs} \\ L_{ds} & 0 \end{bmatrix} \begin{bmatrix} i_{ds}^{\hat{r}} \\ i_{qs}^{\hat{r}} \end{bmatrix} + \begin{bmatrix} 0 \\ \hat{\omega}_r \lambda_f \end{bmatrix} + \begin{bmatrix} \tilde{e}_{ds}^{\hat{r}} \\ \tilde{e}_{qs}^{\hat{r}} \end{bmatrix} \tag{16}$$

where $\begin{bmatrix} \tilde{e}_{ds}^{\hat{r}} \\ \tilde{e}_{qs}^{\hat{r}} \end{bmatrix} = \begin{bmatrix} \lambda_{\omega,d} \\ \lambda_{\omega,q} \end{bmatrix} \tilde{\omega}_r + \begin{bmatrix} \lambda_{p\theta,d} \\ \lambda_{p\theta,q} \end{bmatrix} p\tilde{\theta}_r + \begin{bmatrix} e_{\theta,d} \\ e_{\theta,q} \end{bmatrix} \tilde{\theta}_r, \begin{bmatrix} \lambda_{\omega,d} \\ \lambda_{\omega,q} \end{bmatrix} = \begin{bmatrix} -L_{qs} i_{qs}^{\hat{r}} \\ L_{ds} i_{ds}^{\hat{r}} + \lambda_f \end{bmatrix}, \begin{bmatrix} \lambda_{p\theta,d} \\ \lambda_{p\theta,q} \end{bmatrix} = \begin{bmatrix} L_{ds} i_{qs}^{\hat{r}} \\ -L_{qs} i_{ds}^{\hat{r}} \end{bmatrix},$

$$\begin{bmatrix} e_{\theta,d} \\ e_{\theta,q} \end{bmatrix} = \begin{bmatrix} -\hat{\omega}_r \lambda_f - 2\Delta L_s(\hat{\omega}_r i_{ds}^{\hat{r}} - p i_{qs}^{\hat{r}}) \\ 2\Delta L_s(\hat{\omega}_r i_{qs}^{\hat{r}} + p i_{ds}^{\hat{r}}) \end{bmatrix}.$$

$$H_{\theta\theta} = \frac{\left(L_{\gamma\theta}s^2 + L_{\theta\theta}s + L_{\theta\gamma}L_{\gamma\theta}\right)H_2(s) + (1-L_{\gamma\theta})\left\{H_3(s) + s^2\left\{\frac{J_m}{\hat{J}_m}s^2 + \left(\frac{B_m}{\hat{J}_m} + L_{\gamma P}\right)s + {L_{\gamma I}}'\right\}\right\}}{H_1(s)H_2(s) + (1-L_{\gamma\theta})H_3(s)}$$

$$H_{\theta T} = \frac{(1-L_{\gamma\theta})\frac{P}{2\hat{J}_m}s^2}{H_1(s)H_2(s) + (1-L_{\gamma\theta})H_3(s)}, \quad H_{\omega\omega} = \frac{H_1(s)\left\{\frac{J_m}{\hat{J}_m}s^2 + \left(\frac{B_m}{\hat{J}_m} + L_{\gamma P}\right)s + {L_{\gamma I}}'\right\} + (1-L_{\gamma\theta})H_3(s)}{H_1(s)H_2(s) + (1-L_{\gamma\theta})H_3(s)},$$

$$H_{\omega T} = \frac{H_1(s)\frac{P}{2\hat{J}_m}s}{H_1(s)H_2(s) + (1-L_{\gamma\theta})H_3(s)} \tag{17}$$

where $H_1(s) = s^2 + L_{\theta\theta}s + L_{\theta\gamma}L_{\gamma\theta}$, $H_2(s) = s^2 + \left(\frac{\hat{B}_m}{\hat{J}_m} + L_{\gamma P}\right)s + {L_{\gamma I}}'$,

$H_3(s) = L_{\theta P}s^2 + (L_{\gamma P}L_{\theta\gamma} + {L_{\theta I}}')s + {L_{\gamma I}}'L_{\theta\gamma}$.

REFERENCES

[1] J.-H. Jang, J.-I. Ha, M. Ohto, K. Ide, and S.-K. Sul, "Analysis of permanent-magnet machine for sensorless control based on high-frequency signal injection," *IEEE Trans. Ind. Appl.*, vol. 40, no. 6, pp. 1595–1604, Nov./Dec. 2004.

[2] Y. Li, Z. Q. Zhu, D. Howe, C. M. Bingham, and D. A. Stone, "Improved rotor-position estimation by signal injection in brushless AC motors, accounting for cross-coupling magnetic saturation," *IEEE Trans. Ind. Appl.*, vol. 45, no. 5, pp. 1843–1850, Sep./Oct. 2009.

[3] M. W. Degner and R. D. Lorenz, "Using multiple saliencies for the estimation of flux, position, and velocity in AC machines," *IEEE Trans. Ind. Appl.*, vol. 34, no. 5, pp. 1097–1104, Sep./Oct. 1998.

[4] P. Guglielmi, M. Pastorelli, and A. Vagati, "Cross-saturation effects in IPM motors and related impact on sensorless control," *IEEE Trans. Ind. Appl.*, vol. 42, no. 6, pp. 1516–1522, Nov./Dec. 2006.

[5] Y.-D. Yoon, S.-K. Sul, S. Morimoto, and K. Ide, "High-bandwidth sensorless algorithm for AC machines based on square-wave-type voltage injection," *IEEE Trans. Ind. Appl.*, vol. 47, no. 3, pp. 1361–1370, May/Jun. 2011.

[6] D. Kim, Y.-C. Kwon, S.-K. Sul, J.-H. Kim, and R.-S. Yu, "Suppression of injection voltage disturbance for high-frequency square-wave injection sensorless drive with regulation of induced high-frequency current ripple," *IEEE Trans. Ind. Appl.*, vol. 52, no. 1, pp. 302–312, Jan./Feb. 2016.

[7] L. M. Gong and Z. Q. Zhu, "A novel method for compensating inverter nonlinearity effects in carrier signal injection-based sensorless control from positive-sequence carrier current distortion," *IEEE Trans. Ind. Appl.*, vol. 47, no. 3, pp. 1283–1292, May/Jun. 2011.

[8] G. Wang, R. Yang, and D. Xu, "DSP-based control of sensorless IPMSM drives for wide-speed-range operation," *IEEE Trans. Ind. Electron.*, vol. 60, no. 2, pp. 720–727, Feb. 2013.

[9] C. Silva, G. M. Asher, and M. Sumner, "Hybrid rotor position observer for wide speed-range sensorless PM motor drives including zero speed," *IEEE Trans. Ind. Electron.*, vol. 53, no. 2, pp. 373–378, Apr. 2006.

[10] Y. Sun, M. Preindl, S. Sirouspour, and A. Emadi, "Unified wide-speed sensorless scheme using nonlinear optimization for IPMSM drives," *IEEE Trans. Power Electron.*, vol. 32, no. 8, pp. 6308–6322, Aug. 2017.

[11] B. Du, S. Wu, S. Han, and S. Cui, "Application of linear active disturbance rejection controller for sensorless control of internal permanent-magnet synchronous motor," *IEEE Trans. Ind. Electron.*, vol. 63, no. 5, pp. 3019–3027, May 2016.

[12] Y. Inoue, K. Yamada, S. Morimoto, and M. Sanada, "Effectiveness of voltage error compensation and parameter identification for model-based sensorless control of IPMSM," *IEEE Trans. Ind. Appl.*, vol. 45, no. 1, pp. 213–221, Jan./Feb. 2009.
[13] G. Wang, H. Zhan, G. Zhang, X. Gui, and D. Xu, "Adaptive compensation method of position estimation harmonic error for EMF-based observer in sensorless IPMSM drives," *IEEE Trans. Power Electron.*, vol. 29, no. 6, pp. 3055–3064, Jun. 2014.
[14] Y. Zhao, W. Qiao, and L. Wu, "Dead-time effect analysis and compensation for a sliding-mode position observer-based sensorless IPMSM control system," *IEEE Trans. Ind. Appl.*, vol. 51, no. 3, pp. 2528–2535, May/Jun. 2015.
[15] K.-W. Lee and J.-I. Ha, "Evaluation of back-EMF estimators for sensorless control of permanent magnet synchronous motors," *J. Power Electron.*, vol. 12, no. 4, pp. 604–614, Jul. 2012.
[16] Y. Lee, Y.-C. Kwon, and S.-K. Sul, "Comparison of rotor position estimation performance in fundamental-model-based sensorless control of PMSM," in *Proc. IEEE Energy Convers. Congr. Expo.*, Sep. 20–24, 2015, pp. 5624–5633.
[17] K. Lu, X. Lei, and F. Blaabjerg, "Artificial inductance concept to compensate nonlinear inductance effects in the back-EMF-based sensorless control method for PMSM," *IEEE Trans. Energy Convers.*, vol. 28, no. 3, pp. 593–600, Sep. 2013.
[18] I. Boldea, M. C. Paicu, and G.-D. Andreescu, "Active flux concept for motion-sensorless unified AC drives," *IEEE Trans. Power Electron.*, vol. 23, no. 5, pp. 2612–2618, Sep. 2008.
[19] Y. Zhao, Z. Zhang, W. Qiao, and L. Wu, "An extended flux model-based rotor position estimator for sensorless control of salient-pole permanent-magnet synchronous machines," *IEEE Trans. Power Electron.*, vol. 30, no. 8, pp. 4412–4422, Aug. 2015.
[20] S. Morimoto, K. Kawamoto, M. Sanada, and Y. Takeda, "Sensorless control strategy for salient-pole PMSM based on extended EMF in rotating reference frame," *IEEE Trans. Ind. Appl.*, vol. 38, no. 4, pp. 1054–1061, Jul./Aug. 2002.
[21] Z. Chen, M. Tomita, S. Doki, and S. Okuma, "An extended electromotive force model for sensorless control of interior permanent-magnet synchronous motors," *IEEE Trans. Ind. Electron.*, vol. 50, no. 2, pp. 288–295, Apr. 2003.
[22] M. S. Rafaq, F. Mwasilu, J. Kim, H. H. Choi, and J.-W. Jung, "Online parameter identification for model-based sensorless control of interior permanent magnet synchronous machine," *IEEE Trans. Power Electron.*, vol. 32, no. 6, pp. 4631–4643, Jun. 2017.
[23] H. Kim, M. C. Harke, and R. D. Lorenz, "Sensorless control of interior permanent-magnet machine drives with zero-phase lag position estimation," *IEEE Trans. Ind. Appl.*, vol. 39, no. 6, pp. 1726–1733, Nov./Dec. 2003.
[24] T. Senjyu, T. Shingaki, and K. Uezato, "Sensorless vector control of synchronous reluctance motors with disturbance torque observer," *IEEE Trans. Ind. Electron.*, vol. 48, no. 2, pp. 402–407, Apr. 2001.
[25] W. Sun, J. Gao, Y. Yu, G. Wang, and D. Xu, "Robustness improvement of speed estimation in speed-sensorless induction motor drives," *IEEE Trans. Ind. Appl.*, vol. 52, no. 3, pp. 2525–2536, May/Jun. 2016.
[26] J. Choi, K. Nam, A. A. Bobtsov, A. Pyrkin, and R. Ortega, "Robust adaptive sensorless control for permanent-magnet synchronous motors," *IEEE Trans. Power Electron.*, vol. 32, no. 5, pp. 3989–3997, May 2017.
[27] Y. Lee and S.-K. Sul, "Model-based sensorless control of IPMSM enhancing robustness based on the estimation of speed error," in *Proc. 2016 IEEE Symp. Sensorless Control Elect. Drives*, Jun. 5–6, 2016, pp. 46–53.
[28] N. Matsui, "Sensorless PM brushless DC motor drives," *IEEE Trans. Ind. Appl.*, vol. 43, no. 2, pp. 300–308, Apr. 1996.
[29] N. Matsui, T. Takeshita, and K. Yasuda, "A new sensorless drive of brushless DC motor," in *Proc. Int. Conf. Ind. Electron. Control Instrum.*, Nov. 1992, pp. 430–435.
[30] R. W. Hejny and R. D. Lorenz, "Evaluating the practical low-speed limits for back-EMF tracking-based sensorless speed control using drive stiffness as a key metric," *IEEE Trans. Ind. Appl.*, vol. 47, no. 3, pp. 1337–1343, May/Jun. 2011.
[31] F. Genduso, R. Miceli, C. Rando, and G. R. Galluzzo, "Back-EMF sensorless-control algorithm for high-dynamic performance PMSM," *IEEE Trans. Ind. Electron.*, vol. 57, no. 6, pp. 2092–2100, Jun. 2010.
[32] H. Kim, J. Son, and J. Lee, "A high-speed sliding-mode observer for the sensorless speed control of a PMSM," *IEEE Trans. Ind. Electron.*, vol. 58, no. 9, pp. 4069–4077, Sep. 2011.
[33] H. A. A. Awan, T. Tuovinen, S. E. Saarakkala, and M. Hinkkanen, "Discrete-time observer design for sensorless synchronous motor drives," *IEEE Trans. Ind. Appl.*, vol. 52, no. 5, pp. 3968–3979, Sep./Oct. 2016.
[34] M. Hinkkanen, T. Tuovinen, L. Harnefors, and J. Luomi, "A combined position and stator-resistance observer for salient PMSM drives: design and stability analysis," *IEEE Trans. Power Electron.*, vol. 27, no. 2, pp. 601–609, Feb. 2012.
[35] W.-S. Huang, C.-W. Liu, P.-L. Hsu, and S.-S. Yeh, "Precision control and compensation of servomotors and machine tools via the disturbance observer," *IEEE Trans. Ind. Electron.*, vol. 57, no. 1, pp. 420–429, Jan. 2010.
[36] K.-H. Kim and M.-J. Youn, "A nonlinear speed control for a PM synchronous motor using a simple disturbance estimation technique," *IEEE Trans. Ind. Electron.*, vol. 49, no. 3, pp. 524–535, Jun. 2002.
[37] G. Pellegrino, R. I. Bojoi, P. Guglielmi, and F. Cupertino, "Accurate inverter error compensation and related self-commissioning scheme in sensorless induction motor drives," *IEEE Trans. Ind. Appl.*, vol. 46, no. 5, pp. 1970–1978, Sep./Oct. 2010.

Younggi Lee (S'14) was born in South Korea in 1990. He received the B.S. degree in electrical engineering from Seoul National University, Seoul, South Korea, in 2013, where he is currently working toward the Ph.D. degree.

His research interests include power electronics, control of electric machines, electric/hybrid vehicles, and sensorless drive.

Seung-Ki Sul (S'78–M'87—SM'98–F'00) received the B.S., M.S., and Ph.D. degrees in electrical engineering from Seoul National University, Seoul, South Korea, in 1980, 1983, and 1986, respectively.

From 1986 to 1988, he was an Associate Researcher in the Department of Electrical and Computer Engineering, University of Wisconsin, Madison, WI, USA. From 1988 to 1990, he was a Principal Research Engineer at LG Industrial Systems Company, Seoul. Since 1991, he has been a Member of Faculty with the School of the Electrical and Computer Engineering, Seoul National University, where he is currently a Professor. He has authored or co-authored more than 150 IEEE journal papers and a total of more than 340 international conference papers in the area of power electronics. He holds 14 U.S. patents, seven Japanese patents, 11 Korean patents, and has supervised 43 Ph.D. students. His research interests include power electronic control of electrical machines, electric/hybrid vehicles and ship drives, high-voltage dc transmission based on modular multilevel converter, and power-converter circuits for renewal energy sources.

Dr. Sul was the Program Chair of the IEEE Power Electronics Specialists Conference'06 and the General Chair of the IEEE Energy Conversion Congress and Exposition-Asia and the International Conference on Power Electronics, 2011. In 2015, he was the President of the Korean Institute of Power Electronics. He was the recipient of the 2015 IEEE TRANSACTIONS first and second paper awards on industrial applications, simultaneously. He was also the recipient of the 2016 Outstanding Achievement Award from the IEEE Industrial Application Society and the 2017 Newell Award from the IEEE Power Electronics Society.